J Mater Sci (2011) 46:6191–6202
DOI 10.1007/s10853-011-5382-2

ABBASCHIAN FESTSCHRIFT

Dynamics of interface pattern formation in 3D alloy solidification: first results from experiments in the DECLIC directional solidification insert on the International Space Station

Nathalie Bergeon · Anthony Ramirez · Liang Chen · Bernard Billia · Jiho Gu · Rohit Trivedi

Received: 29 October 2010 / Accepted: 8 February 2011 / Published online: 24 February 2011

Abstract One of the critical microstructures in directional solidification of alloys is the cellular/dendritic pattern that governs the properties and reliability of the solidified material. Our quantitative understanding of the solid–liquid interface pattern has come mainly from experiments in thin samples where the microstructure selection is shown to occur during the dynamical growth process. A more realistic configuration is to examine the evolution of microstructure in three-dimensions, which is not possible terrestrially since convection effects dominate in bulk samples and prevent precise characterization of microstructure dynamics. Recently, experiments under low gravity conditions have been carried out jointly by NASA and CNES in the model transparent system succinonitrile–camphor on board the International Space Station using the Directional Solidification Insert in the DECLIC facility. After a brief description of the experimental setup and methods, the first results on dynamics of interface pattern formation obtained in microgravity will be presented and the information extracted from their quantitative analysis will be discussed.

N. Bergeon (✉) · A. Ramirez · L. Chen · B. Billia
Faculté des Sciences et Techniques, Campus de Saint-Jérôme, Aix-Marseille Université, IM2NP, Avenue Escadrille Normandie Niemen-Case 142, F-13397 Marseille Cedex, France
e-mail: Nathalie.bergeon@im2np.fr

N. Bergeon · A. Ramirez · L. Chen · B. Billia
Faculté des Sciences et Techniques, Campus de Saint-Jérôme, CNRS, IM2NP (UMR 6242), Avenue Escadrille Normandie Niemen-Case 142, F-13397 Marseille Cedex, France

J. Gu · R. Trivedi
Department of Materials Science and Engineering and Ames Laboratory-USDO, Iowa State University, Ames, IA 50011, USA

Introduction

The study of solidification microstructure formation is very important in the design and processing of new materials [1]. The interface patterns formed by solidification largely govern mechanical and physical properties of materials, so that materials and processing conditions can be designed to obtain specific patterns which give optimum properties and better reliability of the finished product. For example, the properties and the reliability of materials processed by all important commercial solidification techniques, such as continuous casting and laser welding, are governed by the microstructural characteristics of cells and dendrites. Directional solidification is a powerful technique to study pattern formation since the growth parameters can be accurately controlled.

One of the key problems in pattern evolution is the prediction of the specific pattern developed under given growth conditions. Pattern selection occurs under dynamic conditions of growth in which the unstable pattern goes through the process of reorganization into a rather periodic array. In situ observation of the solid–liquid interface is a precious tool to get a detailed knowledge of the entire time evolution of the interface pattern. This explains the very extensive use of transparent organic analogs that behave like metallic alloys regarding solidification but are transparent to visible light so that classical optical techniques are sufficient for their observation [2].

Extensive ground-based studies carried out in metallic and organic bulk samples have clearly established the presence of significant convection under the growth conditions which give rise to cellular and dendritic structures. Fluid flow modifies the structure of the solute boundary layer by sweeping thus causing non-uniform morphological instability [3, 4] with the formation of a non-uniform

microstructure. Fluid flow elimination on earth can be obtained by reducing the size of samples. Many experiments on transparent systems have been conducted either on thin samples (quasi-2D shape) [5–8] or in capillary tubes [9]. Even if such configurations have led to very large progress in understanding the dynamics of solidification, they do not perfectly represent 3D samples and quantitative data extracted from 2D systems can not be extrapolated to 3D ones [10]. Recent numerical results of Gurevich et al. [11] using rigorous phase-field models stress this difference. They point out, for example, that 2D simulations give different characteristics compared to 3D ones in terms of cell tip undercooling and steady-state branches of microstructures. Bulk experiments are therefore required but, because of fluid flow, no reliable experimental data are available to sustain the sound quantitative analysis for bulk sample growth in the cellular and dendritic regimes. Fluid flow elimination in 3D samples demands the reduced-gravity environment of space. The study presented here was conducted using the Directional Solidification Insert (DSI) dedicated to in situ and real-time characterization of the dynamical selection of the solid–liquid interface morphology on BULK samples of transparent materials. It has been developed by the French Space Agency (CNES) in the frame of the DEvice for the study of Critical LIquids and Crystallization project (DECLIC) and it is installed within the International Space Station (ISS) to benefit from a microgravity environment.

The DECLIC facility is a compact, multi-user facility for conducting experiments in the fields of fluid physics and materials science, and more generally on transparent media, within the ISS environment. The main part of the facility is common to all experiments and mainly contains electronics (for regulation, data acquisition and management, communication…) and some optical resources (laser, optics, cameras). Three different inserts that contain elements specific to each topic (and especially specimen cartridges) complete the facility: two of them are dedicated to the study of critical fluids; the third one, called DSI (Directional Solidification Insert) is for solidification. The DECLIC facility of CNES was launched with 17-A shuttle flight (August 2009) as part of a joint NASA/CNES research program. The main instrument monitoring is made from the CADMOS center, the French User Support and Operation Centre (USOC) in Toulouse. Taking advantage of provided tele-science capabilities, scientists have the possibility to follow in near real-time conditions and to remotely control experiments. The commissioning of the instrument with the DSI was realized from 7 to 11th of December 2009 and the results obtained during this very first set of experiments will be detailed here.

Before entering into quantitative and precise elements, we should point out the most striking characteristic of the patterns grown in microgravity that fully justifies the need of such environment. In contradistinction with 3D ground patterns, the microgravity ones are very homogeneous as illustrated in Fig. 1. The ground pattern (Fig. 1a) is characterized by a very clear radial variation of size going from large cells in the center to small cells and even smooth interface at the crucible border; this variation is due to convection that induces radial gradients in the microstructure control parameters along the interface [3]. As expected, removing convection drastically reduces such heterogeneity as radial variation of size is no longer noticeable anymore on the pattern grown in microgravity (Fig. 1b). In this last case, the width of the size histogram is then fully representative of the selection process (Fig. 1c).

After a brief description of the experimental procedure, we will detail the methods of analysis of images that have been developed for treating the huge amount of images generated during such experiments to extract quantitative data. Results will be described in terms of pattern formation and evolution. Quantitative measurements will be

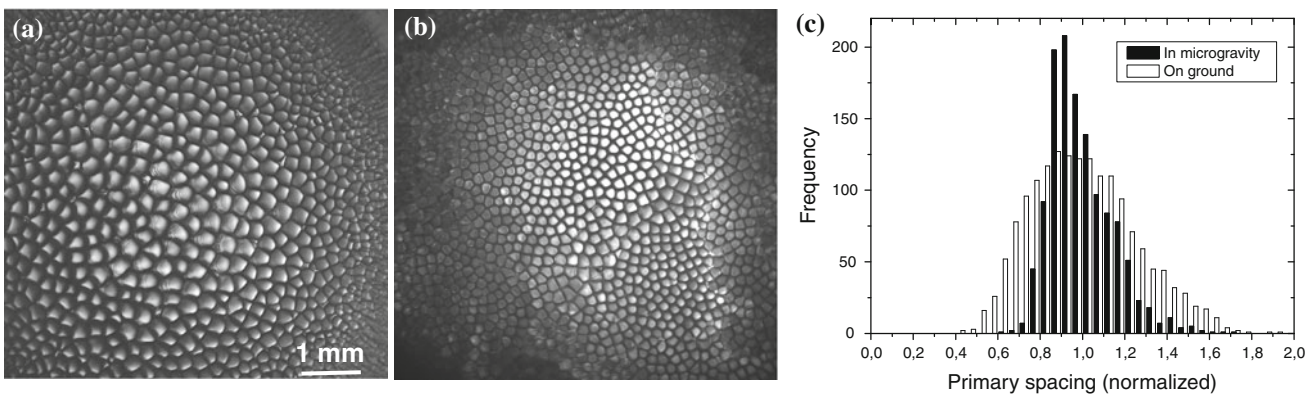

Fig. 1 Comparison between patterns grown **a** on ground (SCN–0.1 wt%, $V_P = 10$ μm/s, $G = 17$ K/cm); **b** in microgravity (SCN–0.24 wt% Camphor, $V_P = 4$ μm/s, $G = 20$ K/cm); and **c** Primary spacing distributions for **a** in white and for **b** in black

compared to ground experiments on thin samples realized for the same alloy and the same thermal conditions.

Experimental procedure

The DECLIC-DSI device

The DSI insert mainly contains two elements: the Bridgman furnace and the experimental cartridge. Some specific optical elements are also included in the insert, even if the main optical parts belong to the common part of DECLIC (LEDs, cameras, laser…). More complete descriptions of DECLIC and its inserts can be found, for example, in [12, 13].

The experimental cartridge includes the quartz crucible and a system of volume compensation made of stainless steel that is useful to accommodate the specimen volume variations associated to phase changes. The cylindrical crucible has an inner diameter of 10 mm and a length that enables about 10 cm of solidification, thus allowing the study of the whole development of extended 3D patterns from their initial stages to the steady state. The crucible is equipped with a flat glass window at the bottom and a lens immersed in the melt at the top. The main observation mode (Axial observation) takes advantage of the complete axial transparency of the cartridge provided by these last two elements: the light coming from LEDs passes through the cartridge from the bottom to the top, therefore crossing the interface. The optical system formed by the immersed lens and a following relay lens form the image of the interface on a CCD camera. On the same cartridge axis, an interferometer is also set but it will not be detailed here (more information on its use can be found in [14]). The interface can also be observed from the side (Transverse observation).

In this study, we use a Succinonitrile (SCN)–0.24 wt% Camphor alloy. The relevant physical data associated to this system are given in Table 1. For filling the crucible, SCN purified by NASA by both distillation and zone melting was used. The alloy was then prepared by adding the solute. All procedures for sample preparation were carefully realized under vacuum to avoid humidity contamination. Once sealed, the cartridge has been inserted inside the Bridgman furnace.

Table 1 Relevant physical data for Succinonitrile (SCN) and SCN–0.24 wt% Camphor (from [27])

Melting point of pure SCN (T_M)	331.24 K
Liquidus slope (m_L)	−1.365 K/wt%
Partition coefficient (k)	0.2
Diffusion coefficient in liquid (D_L)	0.23×10^{-9} m^2/s

A thermal gradient ranging from 10 to 30 K/cm is imposed by regulated hot and cold zones, respectively, located above and below the adiabatic area where the interface is positioned. Upward solidification is achieved by pulling the crucible down into the cold zone of the furnace at a rate ranging from 0.1 to 30 μm/s.

In transparent SCN alloys, the glass ampoule conducts heat better than the liquid and solid phases, so that the sample near the wall is cooler than in the center. This temperature difference drives a concavity of the interface. In case of convection, concavity is enhanced by solute accumulation at the center of the depression where fluid flow is ascending; that causes non-uniform morphological instability, and eventually a non-uniform microstructure [3]. However, even in diffusive conditions, concavity is associated to variations of the direction and the value of the thermal gradient along the interface so that non-uniform microstructure may also develop [15], especially in dendritic growth. Control of interface curvature is thus achieved by mean of a booster heater located at the level of the solidification front to inject heat locally and compensate latent heat evacuation [10]; the temperature of the booster heater is adjusted to flatten as much as possible the solid–liquid interface.

For a defined alloy concentration, varying the thermal gradient or more conveniently, the pulling rate, leads to the development of various interface morphologies, ranging from planar front (high gradient—low pulling rate) to cellular and finally dendritic pattern (low gradient—high pulling rate). In the case of dendrites, the growth direction is strongly influenced by the crystal orientation. Without taking care of that fact, the starting fully melted sample solidifies into a polycrystal which exhibits a diversity of grains of random orientations. As dendrites grow along <100> directions in the cubic system, their growth axis is tilted compared to the optical axis for most of the grains; it is mandatory to avoid this situation to enable a quantitative characterization of the dendrite tip. It is thus necessary to grow a single crystal with one <100> direction parallel to the crucible axis, i.e., parallel to the observation axis. In that case, the dendrites, which behave like optical fibers, are neatly seen from the top by illumination through the sample axis. The technique we have developed to grow such single crystals is described in [16] and has been used to prepare the sample studied here.

Experimental procedure

We will mainly present here results obtained during the commissioning period. The experimental time was limited so that we could perform only one solidification of the whole sample. The scientific goal of this experiment was to assess our experimental conditions, and to try to explore

the range of possible microstructures (small amplitude cells, deep cells, and dendrites).

Based on preliminary studies, the temperatures of the different thermal areas, including the temperature of the booster heater, have been set to impose a thermal gradient of the order of 20 °C/cm and adjusted at the beginning of experiment to locate the interface roughly in the middle of the adiabatic area. Partial melting is then performed (A solid seed of ~20 mm is always kept to preserve the single crystal of selected orientation). Stabilization of 24 h is then realized before triggering solidification. The experiment consisted in three steps of solidification of 20-mm length at different pulling rates V_P: 4, 1, and finally 8 μm/s. It was initially foreseen to move on to each step without any break but a software bug led us to stop during 20 min between the first two pulling rates and 3 min between the two last ones.

An experimental determination of the thermal gradient G at the interface has been performed during the following runs. The method is to measure the displacement of the interface Δz associated to a small shift ΔT of the control temperatures of hot and cold areas: $G = \Delta T/\Delta z$. Measurements are performed at rest, and all changes are supposed to be small enough so that the interface stands in the same area of thermal field. In our case, considering the location of the interface (see Fig. 2a), the control area are the hot zone and the booster heater so that the thermal shift was applied to these areas. For $\Delta T = 2.1 \pm 0.1$ °C, we measured $\Delta z = 1.04 \pm 0.05$ mm (compare Fig. 2b and c). The experimental gradient G_{exp} is then 20 ± 2 °C/cm.

Added to its practical utility, this value is also used to evaluate the validity of the numerical CrysVUn® modeling. The CrysVUn® software is designed for the global modeling of solidification processes [17, 18]. Calculations are based on a method of finite volumes on unstructured grids that enables to tackle the entire growth setup on the basis of a geometrical model of the furnace, crucible and sample and assignment of the relevant physical properties to all materials involved in this setup. The temperatures applied to the different elements of the furnace, pulling rates and sample composition are entered as input parameters for the numerical simulations. The modeling of our furnace is a very precious tool to plan but also to analyze experiments. The CrysVUn® modeling of the experimental conditions used led to a thermal gradient of 19.5 °C/cm in the center of the crucible and 18.5 °C/cm on the border. Experimental and modeling data are therefore very consistent.

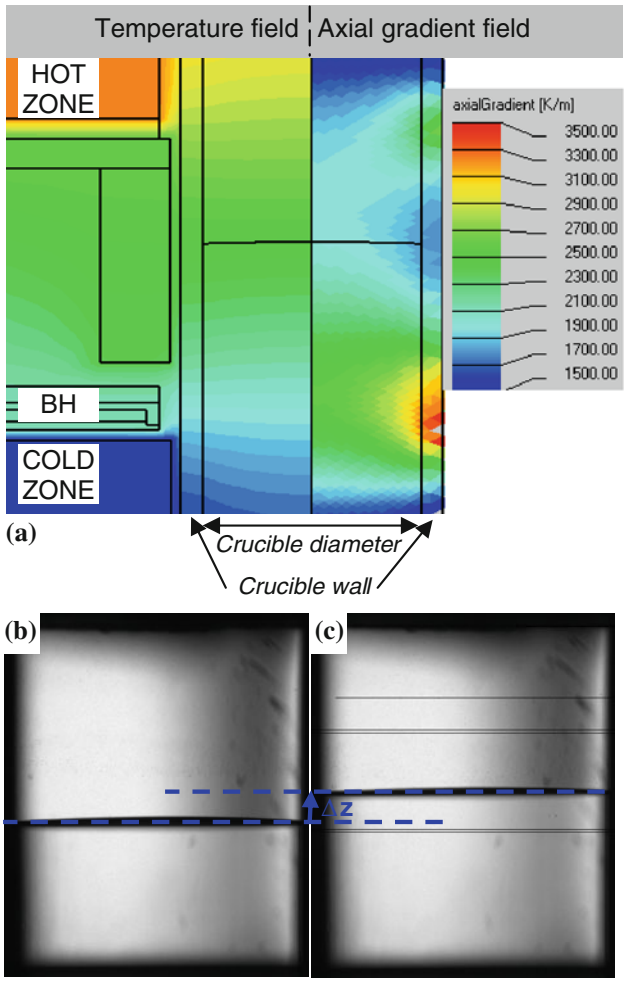

Fig. 2 Thermal gradient measurement **a** Results of CrysVUn modeling figuring the thermal field on the *left*, and the axial gradient field on the *right* in the adiabatic area. **b** Side image of the interface at rest before changing the temperatures of both the booster heater and the hot zone. **c** Side image of the interface at rest after an decrease of 2 °C of both temperatures of the booster heater and the hot zone

Analysis methods

In situ and continuous observation leads to a huge amount of images so that adequate and as systematic as possible procedures had to be developed and validated to extract relevant quantitative data. Quantitative characterization of the patterns consists in measuring the evolution, as a function of time and growth parameters, of the parameters that describe the interface morphology, such as the primary spacing, order/disorder level of pattern, shape of structures, tip radius… Concerning shape of structures and tip radius, measurements are based on interferometric analysis that is not described here as data required to perform these analyses are not yet available (data stored on hard-disk still on ISS, return on ground foreseen beginning of 2011). For more information on shape reconstruction by interferometric analysis in DECLIC-DSI, one may refer to Bergeon et al. [14].

Image treatment and analysis procedures have been developed on both analySIS and Visilog softwares to facilitate exploitation of results. An illustration is given in Fig. 3 by considering a raw image obtained during the

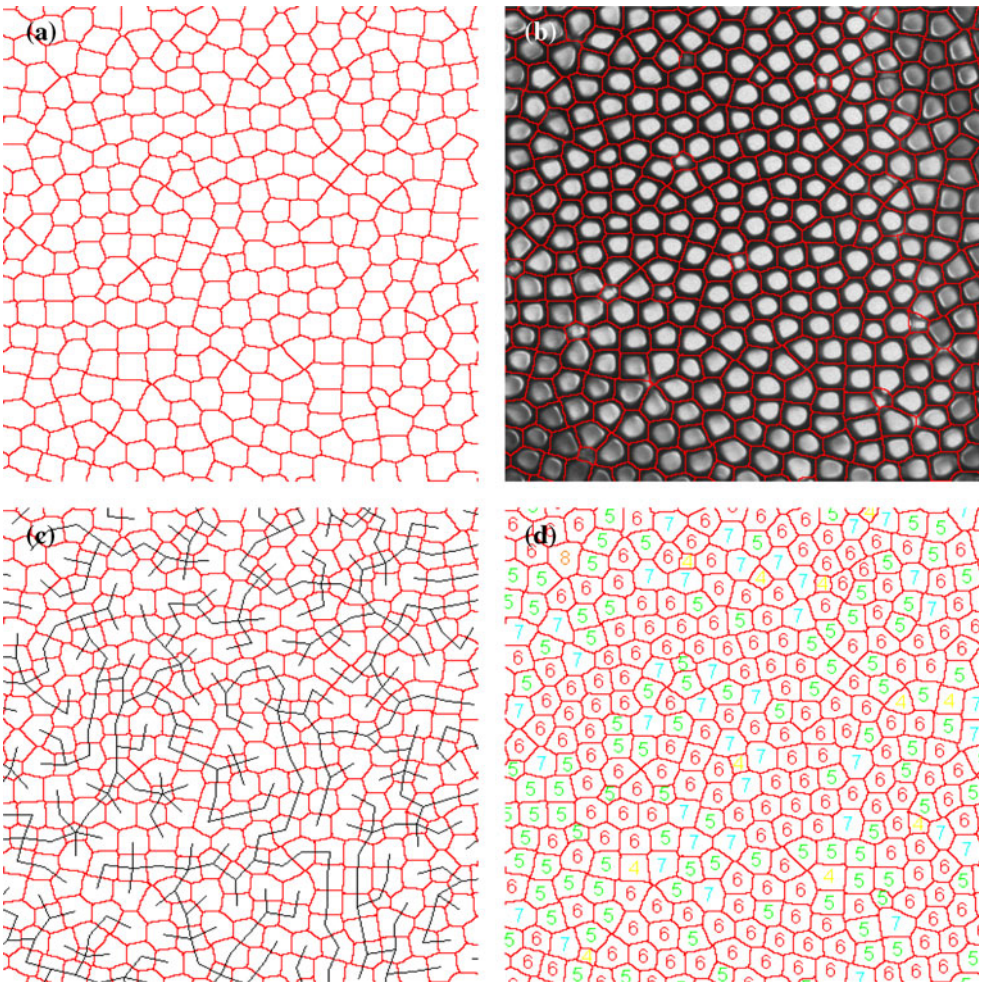

Fig. 3 Procedures of treatment and analysis of images. **a** Binary image; **b** Superimposition of the binary image to the raw image; **c** Minimal Spanning Tree; **d** Number of first neighbors superimposed to the binary image

commissioning experiment. The first step is to obtain a binary image (Fig. 3a) that is, then used as an input for, on the one hand, the cell detection to get the primary spacing distribution, and on the other hand, the use of specific procedures for characterizing pattern order/disorder and type: Minimal Spanning Tree (MST) (Fig. 3c) and number of first neighbors (Fig. 3d).

Primary spacing can be considered as the center to center distance between two consecutive cells. Its determination requires beforehand cell surface measurement. To get this, image treatment and analysis procedures have been developed on both analySIS and Visilog softwares. Treatment of images is necessary as raw images are not directly analyzable. This consists in successive operations aiming first at enhancing the cells outline before obtaining an exploitable binary image. After application of several filters allowing the identification of each cell in the binary image, image analysis can then be performed to determine the primary spacing. In order to validate the developed procedure, superimposition of the treated image to the corresponding raw image is realized as shown in Fig. 3b. The high level of correspondence, which was estimated greater than 90%, allows us to naturally adopt this procedure that is suitable in revealing effectively the cells outline. A Region of Interest (ROI) covering the whole image has been selected for analysis. This zone contains an average of 1000 cells. After detection and identification of every single cell in the selected ROI, each cell surface can be determined by the software. Cells are then assimilated to disks to extract the primary spacing that corresponds to the disk diameter. The histogram of spacing can then be drawn to determine the average spacing and the standard deviation.

The Minimal Spanning Tree (MST) is a tool to characterize and quantify the order hidden behind disorder of any distribution of points on a surface [19]. In our case, points are defined by the centers of cells. The MST is a connected graph without any closed loop, which contains all the centers of cells and for which the sum of the edge lengths is minimum. For a specific pattern, MST construction may not be unique; however, all possible MST are equivalent so that the histogram of edge lengths is unique. Statistical parameters, such as the average edge length m^* and the standard deviation σ^*, deduced from this histogram

then characterize the arrangement of the cell centers. These quantities are normalized following Eq. 1 so that any distribution can be plotted in a (m, σ) diagram and compared to any other 2D arrangement:

$$m = \frac{m^*}{\sqrt{\langle S \rangle}} \frac{N-1}{N}$$
$$\sigma = \frac{\sigma^*}{\sqrt{\langle S \rangle}} \frac{N-1}{N} \quad (1)$$

with $<S>$ average area of cells and N number of cells

The (m, σ) diagram we use (refer to Fig. 9a) already contains points corresponding to two types of well-characterized distributions: hexagonal lattice for a perfectly ordered pattern and uniform random distribution. The path that joins these two extreme cases is obtained by progressive uniform disorder added to the ordered patterns. This method was first applied by Dussert et al. [19] to characterize an aggregated lithium thin film deposited on a dielectric substrate. Then, it was used to analyze cellular patterns resulting from directional solidification in metallic [20] and transparent analog [21] systems as well as by Cerisier et al. [22] to characterize the disorder dynamics of Bénard–Marangoni patterns. The specific procedure to build and analyze MST has been developed using the software Visilog.

Results

Figure 4 provides a step by step description of the whole experiment starting from rest (Fig. 4a).

At $V_P = 4$ μm/s, morphological instability develops quite fast as depicted by linear ridges along sub-boundaries that finally underline a quite complex array. Between these defects, in areas that are still smooth, some poxes appear (Fig. 4b): they can be described as a circular undulation of the interface. Ridges underlining sub-boundaries progressively cut in their transverse directions and simultaneously, a quite uniform corrugation that corresponds to the initial visible wavelength of morphological instability invades the interface (Fig. 4c). The amplitude of all these interface modulations starts to increase, channels are forming but it is still difficult to identify cells (Fig. 4d). At this stage, the dynamic of the interface is extremely fast and the disorder high. There is then a progressive decrease of disorder and a clear pattern of deep cells is eventually reached (Fig. 4e). The dynamics then clearly slows down and limits to progressive size adjustment and ordering (Fig. 4f). These phenomena will be quantitatively described later.

Before triggering the pulling at $V_P = 1$ μm/s, the crucible translation stopped during 20 min so that the microstructure reached at 4 μm/s began to vanish. Yet, disappearance was not complete when pulling restarted (Fig. 4g). The morphological instability appearing was therefore constrained in the remaining traces of the previous pattern (Fig. 4h) but quite surprisingly, instead of growing from the preexisting size, numerous tip splittings occured leading to an initial size largely smaller than the one finally obtained at $V_P = 4$ μm/s. This may be explained by the fact that, even if the previous pattern has not completely vanished, its amplitude has decreased so that previous cell tips can be considered as flat and the process observed is actually similar to morphological instability development on a plane front: the radius of curvature of previous cells is large compared to the wavelength of developing instability. A regular pattern of shallow cells eventually formed of which spacing clearly increased with time before stabilization (Fig. 4i and j).

The break between 1 and 8 μm/s was comparatively small so the new pattern had to develop on the pre-existing large size cellular one, similar to the one of Fig. 4j. Modulations of the pre-existing cell tips appeared quite quickly on the whole pattern (Fig. 4k); these modulations led to the selection of a new tip on the preexisting one and the appearance of secondary branches that progressively grew (Fig. 4l). The dendritic character of the microstructure then became very clear as depicted by the four arms crosses (Fig. 4m). This pattern then evolved slowly to reduce its spacing by tip splitting. This size decrease eventually led to less-developed secondary arms as evidenced in comparing Fig. 4m and n.

Detailed quantitative analyses of these experiments are presented in the following parts.

Interface motion

Throughout the sequence of directional solidifications, macroscopic shape and motion of the interface have been investigated by side view observation. Front recoil with time at two locations at the interface (border and center) as well as the evolution of the interface amplitude which is the distance between the interface position at the two locations considered, have been studied.

At rest, the interface position in the frame of the furnace depends on the thermal field as it is located on the isotherm of the liquidus temperature for the nominal concentration C_0. The macroscopic interface shape is therefore imposed by the shape of the isotherms, and it appears almost flat (refer to Fig. 5a). The height variation or interface amplitude between the center and the border is limited to about 200 μm.

During growth, the build up of the solute boundary layer leads to a progressive change of the equilibrium temperature of the interface that finally reaches the solidus

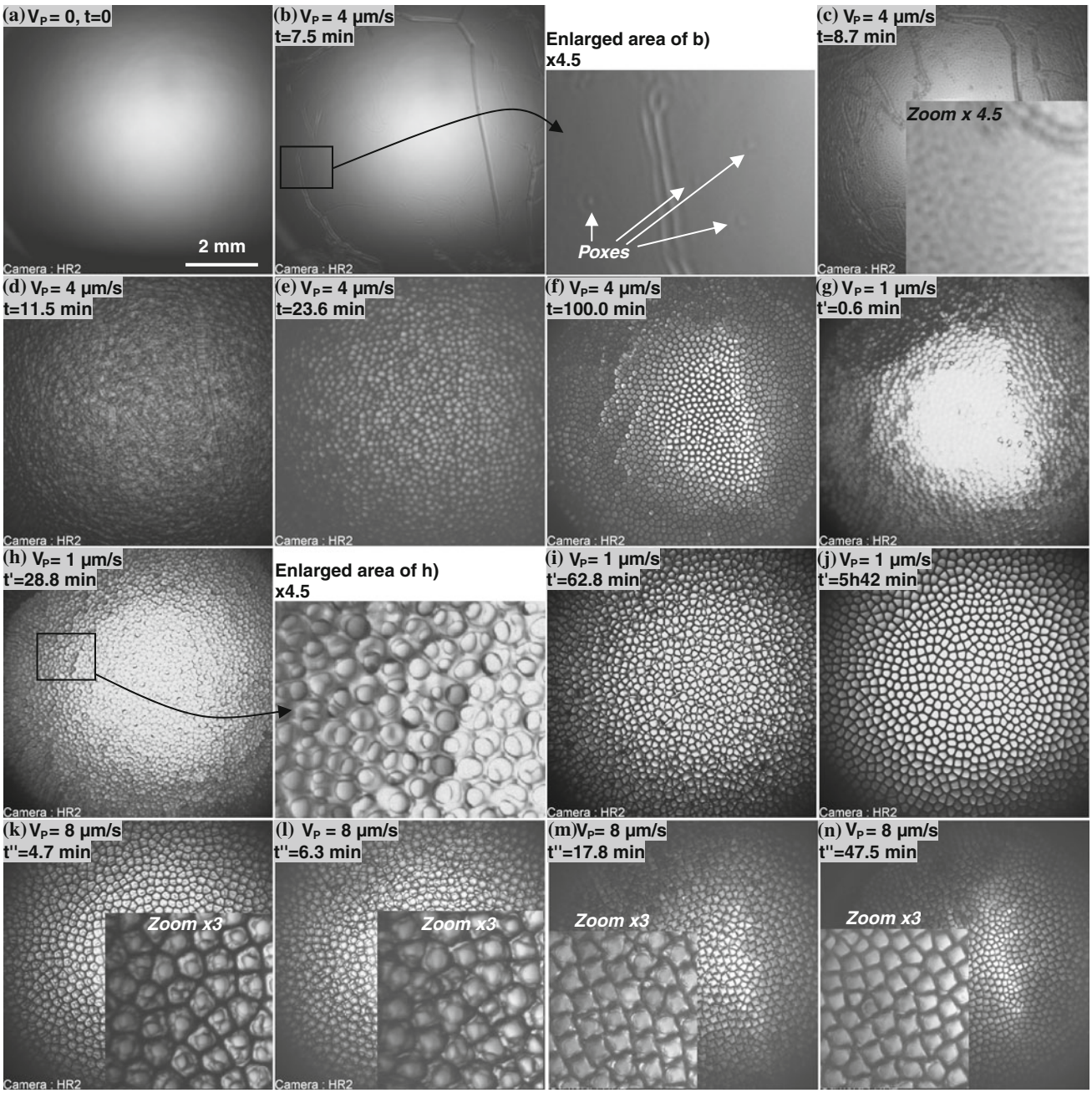

Fig. 4 Microstructure formation and evolution during the whole commissioning experiment. The times t, t', and t'', respectively, start when pullings at 4, 1, and 8 µm/s are triggered

temperature for the same solute concentration C_0. Considering a fixed thermal field characterized by the thermal gradient G, the isotherm change is associated to a front displacement $\Delta z_{WL} = \frac{m_L C_0}{G}\frac{k-1}{k}$, with m_L the liquidus slope and k the partition coefficient (see Table 1). This displacement is evaluated at 653 µm in our case, for the gradient G of 20 K/cm ($C_0 = 0.24$ wt%). It clearly appears from Fig. 5 that the recoil is much more important and moreover, dependent on the pulling rate: it varies from 1.5 mm at $V_P = 1$ µm/s to 4.2 mm for $V_P = 8$ µm/s. This phenomenon is usually not taken into account in theoretical models for front recoil [23–25]. It comes from the low conductivity of SCN compared to that of the crucible wall which is made of glass. Latent heat generation strongly modifies the thermal field, both shifting and curving isotherms. The shift of isotherms explains the additional

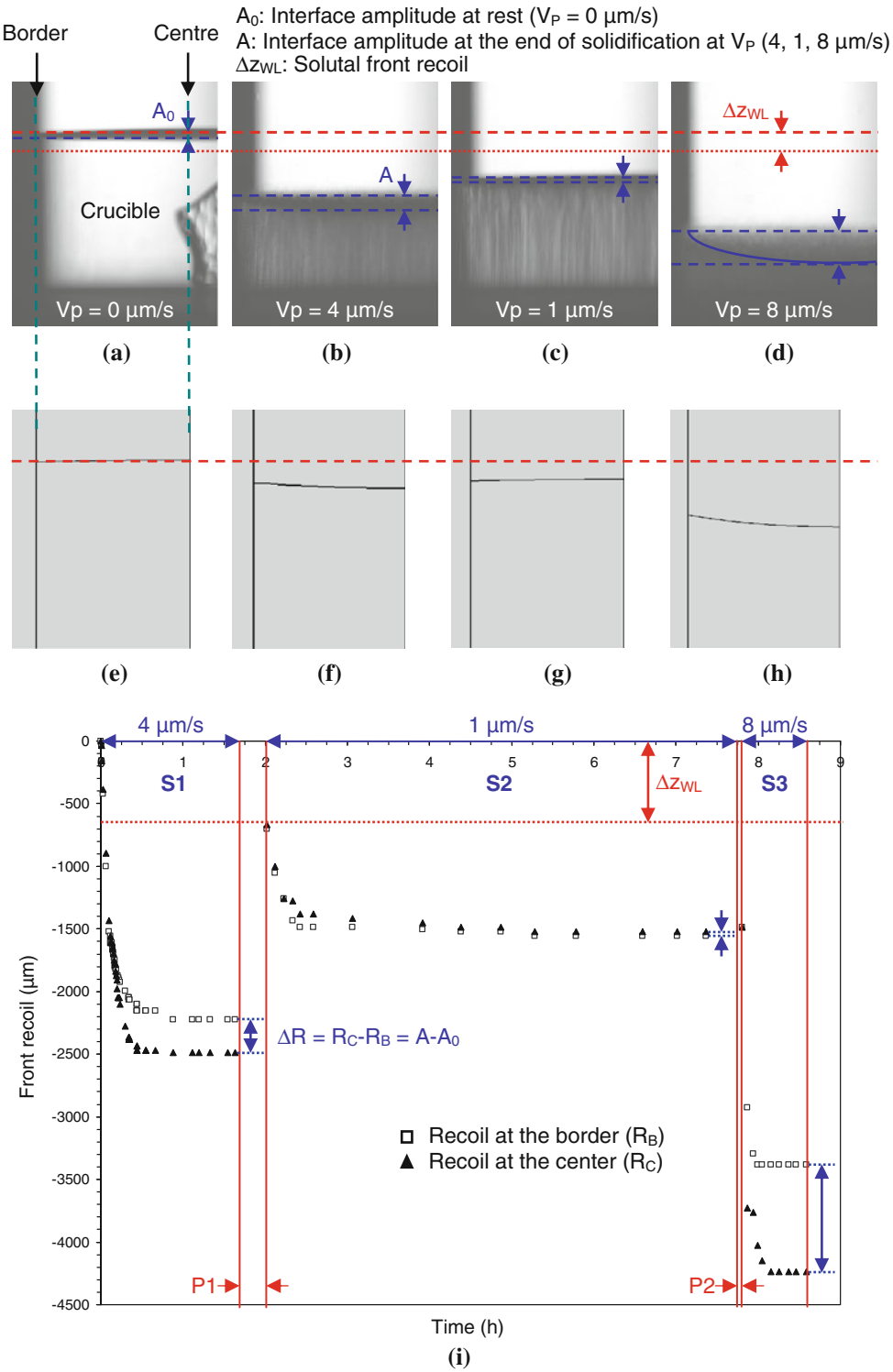

Fig. 5 Evolution of the interface position and amplitude with pulling rate ($V_P = 0$, 4, 1, and 8 µm/s) both experimentally: **a**–**d** and numerically (CrysVUn numerical simulations): **e**–**h**. "*A*" represents the amplitude of the interface which is determined by the upper and lowest interface limits marked by the *two arrows*. An example of the experimental interface shape is drawn in *continuous line* on **d**. The *top large-dots line* corresponds to the initial position of the interface and the *small-dots line* corresponds to the theoretical position of the interface during pulling. **i** Front recoil with time at two locations in the crucible (border and center). *P1* Break of about 20 min between solidifications S1 and S2. *P2* Break of about 3 min between solidifications S2 and S3

recoil; the curvature of isotherms is directly observed in the interface curvature. As latent heat release is proportional to the pulling rate, these effects increase with V_P.

These experimental data can be compared to CrysVUn numerical simulations that are presented in Fig. 5e to h. Figure 5 points out that the experimental and numerical images are qualitatively consistent in terms of recoil and curvature variations : the recoil increases with pulling rate and the interface curvature changes from slightly convex at rest to very weakly convex at 1 µm/s to more and more

concave at 4 and 8 μm/s. Analyzing the thermal field calculated by CrysVUn led us to verify that in all these configurations, the distance between the liquidus and solidus temperatures is about 650 μm so that the larger recoil is due to a global shift of the isotherms downward. Some discrepancies are noted comparing the experimental and numerical amplitudes of recoils: the recoils are underestimated by CrysVUn as we obtain 0.93 mm instead of 1.52 mm for 1 μm/s and 3.22 mm instead of 4.24 for 8 μm/s (center of the interface). More experiments and data are needed to be able to explain and correct these differences but it is worth noting that the comparison of experiments and simulations are not so straightforward: a rigorous comparison would imply comparing the positions of the solidus isotherms in both numerical and experimental data but the experimental position of the solidus temperature is in fact unknown. The experimental interface position is taken arbitrarily at the level of the darkest line (underlined, for example, on Fig. 5d) but its corresponding temperature can not be determined. Moreover, the interface curvature and the cylindrical shape of the crucible do not help the analysis. However, the front recoil in CrysVUn is dominated by thermal recoil and not solutal recoil, as observed in experiments.

Characterization of patterns

The spacing evolution during the whole commissioning experiment has been measured using the procedures described in Analysis methods; the data are presented in Fig. 6.

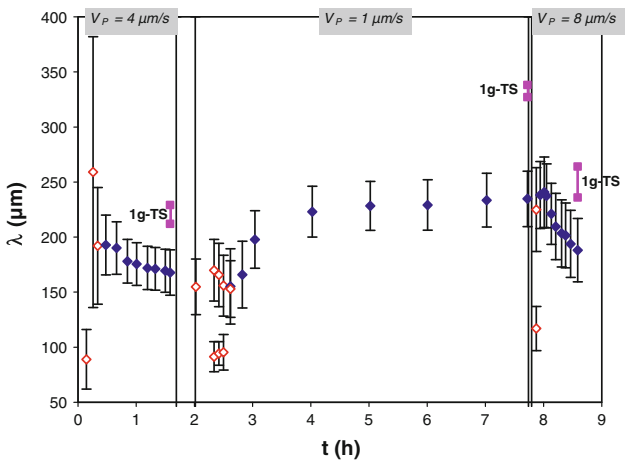

Fig. 6 Primary spacing evolution as a function of time during the whole commissioning experiment. *Open marks* correspond to FFT measurements. For 1 and 8 μm/s, two different wavelengths revealed by FFT, corresponding to two different ranges of spacings, coexist at the same time. The band of spacings for each pulling rate identified as "1g-TS" correspond to comparable ground experiments realized in thin samples (SCN–0.23 wt% Camphor, $G = 17.2$ K/cm)

First of all, it is worth noting that the spacing selection is weak as histograms of spacing always present a band of existing spacing. This band tends to reduce with time as array order increases but it is still large. For the very beginning of the microstructure formation at 4 μm/s, it was not possible to determine the spacing with such methods as microstructure does not form closed cells (images 4c and d for example). So the first two measurements of the Fig. 6 (open marks) have been performed using a FFT (Fast Fourier Transform)-based method. This method is also used for the first measurements at 1 μm/s. In this case, we determine two different wavelengths that correspond to the remaining pattern grown at 4 μm/s (large spacing) and to the morphological instability appearing inside the previous one (small spacing). Those two ranges of spacing eventually collapse in only one range of spacing that starts growing. After the jump from 1 to 8 μm/s, FFT also reveals two different wavelengths that respectively correspond to the remaining pattern traces and the new developing one (image 4k for example) as illustrated in Fig. 7. The internal ring of the FFT (Fig. 7b), associated to large wavelengths, characterizes the deep remaining pattern while the external ring associated to smaller wavelengths characterizes the developing one. The interesting point is that the small wavelength disappears very quickly as only one tip is selected on each splitted tip of Fig. 7a. Growth develops eventually on the pre-existing pattern.

The initial wavelength of instability at $V_P = 4$ μm/s is small and increases very rapidly with time so that spacing presents an overgrowth before decreasing, obviously by tip splitting. This dynamic is consistent with previous observations on thin samples of SCN-based alloys, for example, by Seetharaman et al. [26]. The spacing still seems decreasing when the motion break occurs so that we can conclude that the pattern did not reach its steady-state yet, even if thermal and solutal transients are completed (the front position is stabilized). The same situation occurs for $V_P = 8$ μm/s; spacing seems stabilized only for the part grown at $V_P = 1$ μm/s.

In Fig. 6, points corresponding to comparable ground experiments in thin sample (SCN—0.23 wt% camphor, $G = 17.2$ K/cm) are added. The measurements were performed in stationary state which is not reached in our case, but however, the 2D spacings are significantly larger than the 3D ones. This is consistent, for example, with the phase-field simulations of Gurevich et al. [11] as they reveal that the dimensionality affects quantitatively the branch structure for cells and dendrites. The corresponding images are given in Fig. 8: the branching is developed only for 8 μm/s which is similar with 3D-μg case. Further comparison is foreseen to compare steady-state spacings for the whole range of pulling rates and its history dependence.

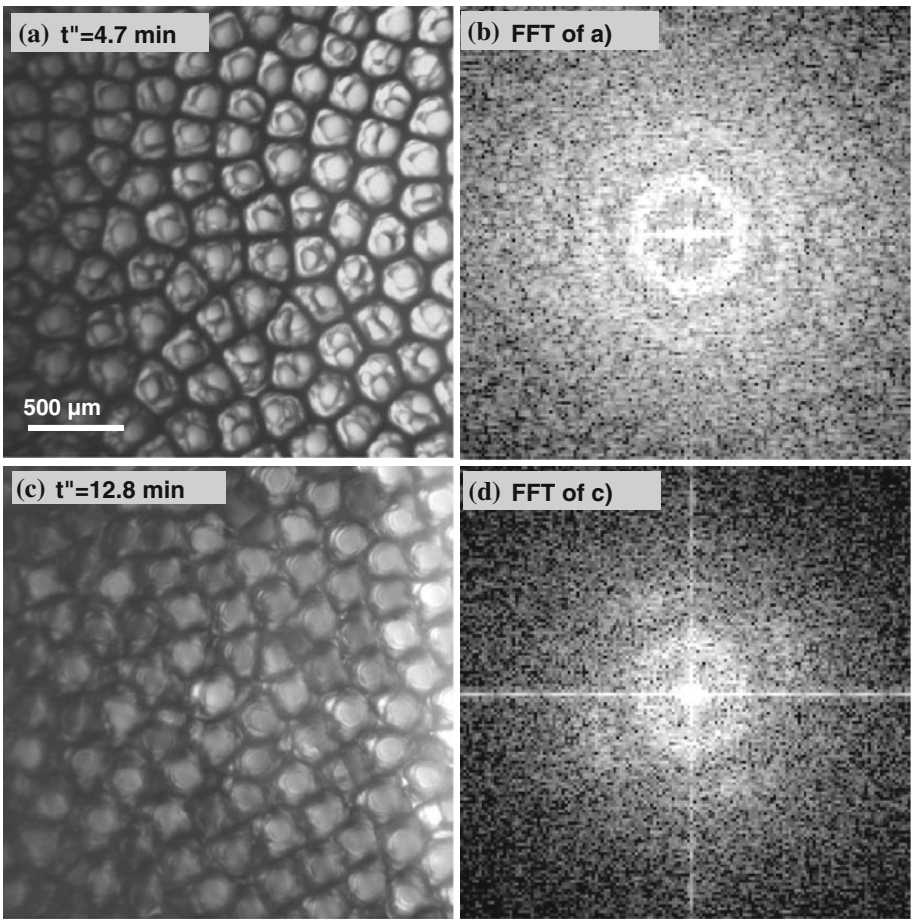

Fig. 7 FFT analysis of some images taken at $V_P = 8$ µm/s. The two rings of **b** correspond to two different ranges of spacing (*open marks* of Fig. 6). The largest ring has disappeared in **d**, the four spots are associated to secondary branches

It is interesting to compare the time evolution of spacing with the corresponding path followed in the (m, σ) diagram built from MST analyses. The results are given in Fig. 9a. All points are located in the vicinity of the line joining the random distribution and the hexagonal tiling. The underlying pattern is always hexagonal, and the time evolution mainly deals with the topological disorder level. First neighbor analyses confirm this point as the number of cells with six neighbors is always largely higher compared to other ones (Fig. 10). A zoom is given in Fig. 9b to better follow the path corresponding to $V_P = 1$ (S2) and 8 µm/s (S3); the final point obtained at 4 µm/s (S1) is also added as a reference. In the earliest stages at 1 µm/s, a very large increase of disorder is observed which is due to the process of development of the instability observed, for example, in Fig. 4h: it describes the birth of a new pattern. A continuous and almost monotonous evolution is then observed at $V_P = 1$ µm/s to reorganize the pattern and go back to the order level obtained in the previous stage at 4 µm/s: the final point at 1 µm/s is very close to the one at 4 µm/s. The evolution at $V_P = 8$ µm/s is more complex. The starting point is for sure close to the final one obtained at 1 µm/s as the velocity jump is almost continuous. The main part of the curve corresponds to large increase of disorder before a short inversion of tendency at the end of the measurement time. The drastic adjustment in primary spacing may explain this evolution as it is associated to a complete reorganization of the array.

Conclusion

In this article, we have detailed the very first results obtained in microgravity during the commissioning experiment of the DSI of the DECLIC device on board ISS. The experimental methods that we have developed to analyze the large amount of images that are generated during such in situ observation have been presented. These methods enable the analysis of both transverse observations to characterize the macroscopic shape and motion of the interface, and direct axial observations, to quantitatively characterize the interface pattern in terms of spacing and quality (order/disorder, number of first neighbors). Complementary measurements with the analysis of interferometric data will be

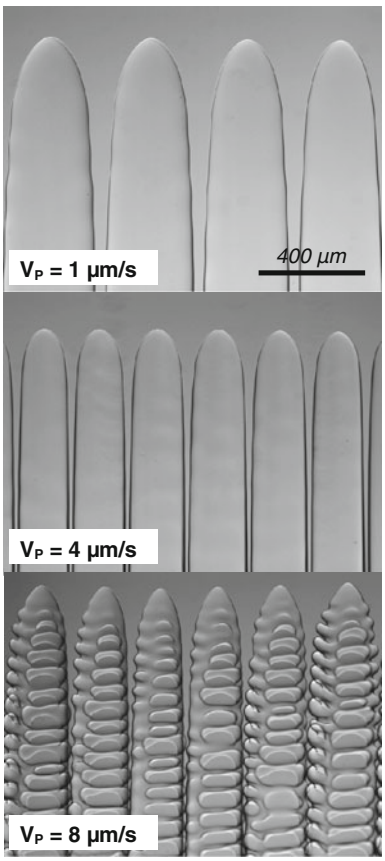

Fig. 8 Steady-state microstructure in thin samples (thickness = 200 µm) as a function of pulling rate (SCN–0.23 wt% Camphor, $G = 17.2$ K/cm)

possible once all data acquired will be downloaded from ISS. Even if this first experiment was limited in duration, the quality of the experimental system that provides very clear images of the interfacial microstructure during its whole evolution has been demonstrated. Microgravity environment has provided the conditions to get quantitative benchmark data: homogeneous patterns corresponding to homogeneous values of control parameters along the whole interface have been obtained.

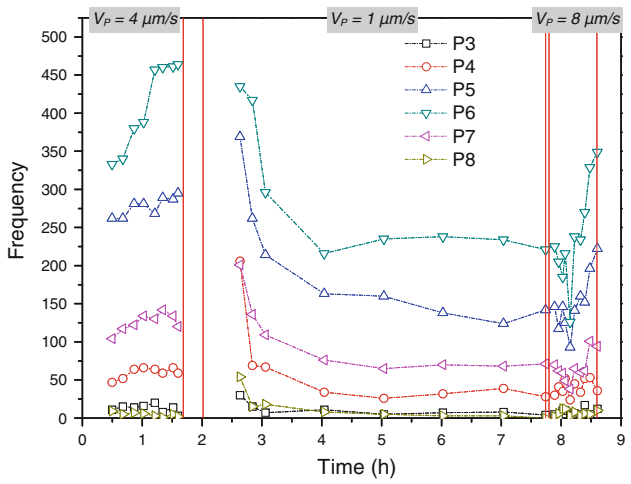

Fig. 10 Evolution of the n-sided polygons (Pn) number versus time during the whole commissioning experiment

Since the commissioning experiment described here, three experimental runs have been performed that roughly represent 50 days of experimental time. In these runs, a large range of experimental conditions have been explored, varying the pulling rate from 0.5 to 16 µm/s for two different thermal gradients. Both long solidifications and solidifications with jumps in pulling rates have been performed to get the whole dynamics and mechanisms of microstructure formation or change, spacing adjustment, pattern ordering… These data are currently under treatment. Simultaneously, similar ground experiments on thin samples are performed to extract the dimensionality influence on both mechanisms and shape characteristics. Finally, numerical 3D phase-field modelings are also currently starting for further analysis and comparison.

Acknowledgements The authors express their gratitude to CNES (Centre National d'Etudes Spatiales) and NASA (National Aeronautics and Space Administration) for the support received in the scientific projects MISOL3D (MIcrostructures de SOLidification 3D) and DSIP (Dynamical Selection of Interface Patterns).

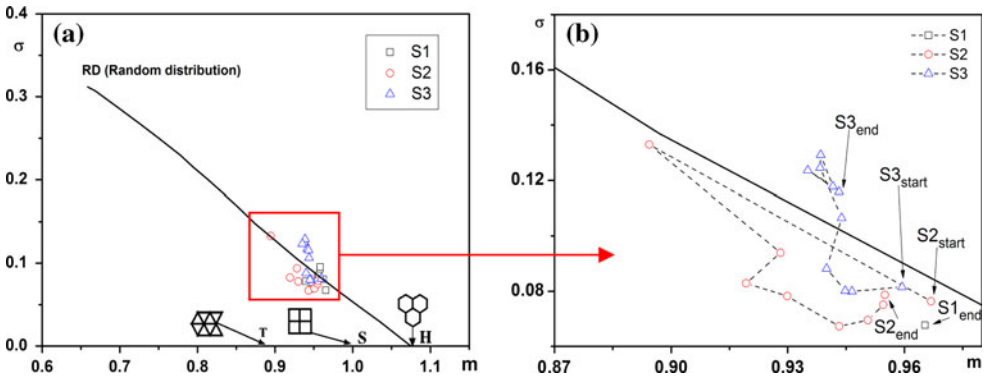

Fig. 9 (m, σ) diagrams gathering the results obtained during the commissioning experiment **a** overall view, **b** enlarged view of the zone located in **a.** *S1* Solidification at $V_P = 4$ µm/s, *S2* Solidification at $V_P = 1$ µm/s, and *S3* Solidification at $V_P = 8$ µm/s

References

1. Billia B, Fecht HJ (2001) In: Fitton B, Battrick B (eds) A world without gravity research in space for health and industrial processes ESA SP 1251. European Space Agency, Noordwijk
2. Billia B, Trivedi R (1993) In: Hurle DTJ (ed) Handbook of crystal growth. vol 1b. North-Holland, Amsterdam
3. Jamgotchian H, Bergeon N, Benielli D, Voge P, Billia B, Guérin R (2001) Phys Rev Lett 87:166105
4. Schenk T, Nguyen Thi H, Gastaldi J, Reinhart G, Cristiglio V, Mangelinck-Noël N, Klein H, Härtwig J, Grushko B, Billia B, Baruchel J (2005) J Cryst Growth 275:201
5. Somboonsuk K, Mason JT, Trivedi R (1984) Metall Trans 15A:967
6. Trivedi R, Somboonsuk K (1985) Acta Metall 33:1061
7. Akamatsu S, Faivre G, Ihle T (1995) Phys Rev E 51:4751
8. Deschamps J, Georgelin M, Pocheau A (2008) Phys Rev E 78: 011605
9. Trivedi R, Han SH, Sekhar JA (1990) In: Rohatgi PK (ed) Solidification of metal–matrix composites. Metallurgical Society of AIME, Warrendale
10. Bergeon N, Trivedi R, Billia B, Echebarria B, Karma A, Liu S, Weiss C, Mangelinck N (2005) Adv Space Res 36:80
11. Gurevich S, Karma A, Plapp M, Trivedi R (2010) Phys Rev E 81:011603
12. Marcout R, Raymond G, Martin B, Cambon G, Zappoli B, Duclos F, Barde S, Beysens D, Garrabos Y, Lecoutre C, Billia B, Bergeon N, Mangelinck N (2006) "DECLIC: a facility to investigate fluids and transparent materials in microgravity conditions in ISS" IAC-06-A2.5.02. In: 57th International Astronautical Congress, 2–6 Oct 2006, Valencia, Spain
13. Pont G, Barde S, Zappoli B, Duclos F, Garrabos Y, Lecoutre C, Beysens D, Billia B, Bergeon N, Mangelinck-Noël N, Marcout R, Blonde D (2009) "DECLIC: a facility to study crystallization and critical fluids" IAC-09-A2.6.4. In: 60th International Astronautical Congress, 12–16 Oct 2009, Daejeon, Republic of Korea
14. Bergeon N, Weiss C, Mangelinck-Noël N, Billia B (2009) Trans Indian Inst Met 62:455
15. Weiss C, Bergeon N, Mangelinck-Noël N, Billia B (2005) Mater Sci Eng A 413–414:296
16. Weiss C, Bergeon N, Mangelinck-Noël N, Billia B (2006) Mater Sci Forum 508:337
17. Kurz M (1998) PhD thesis, Technical University Erlangen-Nürnberg
18. Kurz M, Pusztai A, Müller G (1999) J Cryst Growth 198–199:101
19. Dussert C, Rasigni G, Rasigni M, Palmari J, Llebaria A (1986) Phys Rev B 34:3528
20. Billia B, Jamgotchian H, Nguyen Thi H (1991) Metall Trans A 22:3041
21. Noël N, Jamgotchian H, Billia B (1997) J Cryst Growth 181:117
22. Cerisier P, Rahal S, Billia B (1996) Phys Rev E 54:3508
23. Warren JA, Langer JS (1993) Phys Rev E 47:2702
24. Caroli B, Caroli C, Ramirez-Piscina L (1993) J Cryst Growth 132:377
25. Coriell SR, Boisvert RF, McFadden GB, Brush LN, Favier JJ (1994) J Cryst Growth 140:139
26. Seetharaman V, Eshelman MA, Trivedi R (1988) Acta Metall 36:1175
27. Teng J, Liu S (2006) J Cryst Growth 290:248